Full-field measurements of the microstructure's effect on the mechanical behaviour of a wire and arc additively manufactured duplex stainless steel

Lorenzo Bercelli, Célia Caër, Matthieu Dhondt, Cédric Doudard, Julien Beaudet, Sylvain Calloch

Materials & Design 244 (2024) 113223

Contents lists available at ScienceDirect

Materials & Design

journal homepage: www.elsevier.com/locate/matdes

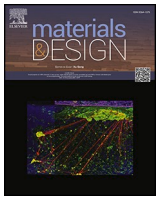

Full-field measurements of the microstructure's effect on the mechanical behaviour of a wire and arc additively manufactured duplex stainless steel

Lorenzo Bercelli [a,*], Célia Caër [a], Matthieu Dhondt [a], Cédric Doudard [a], Julien Beaudet [b], Sylvain Calloch [a]

[a] ENSTA Bretagne, IRDL - UMR CNRS 6027, 29200 Brest, France
[b] Naval Group, Technocampus Océan, 5 rue de l'Halbrane, 44340 Bouguenais, France

ARTICLE INFO

Keywords:
Additive manufacturing
Microstructure
Infrared thermography
Duplex stainless steel
DIC

ABSTRACT

Wire and Arc Additive Manufacturing (WAAM) is particularly well suited to the fabrication of large-scale structural components. Its use for the deposition of Duplex Stainless Steel (DSS) structures is especially sought upon by the naval industry. Although additively manufactured materials usually come with heterogeneous microstructure, residual stresses, internal and surface defects that must not jeopardize the structural integrity of components. In this context, the present study aims to analyse the as-deposited microstructure of a WAAM DSS and its influence on the mechanical behaviour via mechanical field measurement using both Digital Image Correlation (DIC) and Thermoelastic Stress Analysis (TSA).

1. Introduction

Metal Additive Manufacturing (AM) allows for the rapid fabrication of unprecedented designs that meet modern challenges for lighter structural components. Many different technologies of AM exist, and they are adapted to a wide range of metallic alloys [1,2] and scales, from architected materials such as lattice [3,4] to meter-scale structures [5–7]. Among these techniques, Wire and Arc Additive Manufacturing (WAAM) is the best suited to large scale components due to its high material deposition rate of several kilos per hour [8]. WAAM is a direct energy deposition process in which a wire input is melted by an arc onto a substrate, building up the part in a layer-by-layer fashion, each layer being constituted of interlaced weld beads. This process is of particular interest in the naval industry, where it can be used as an alternative to casting for the production of innovative propeller blades [9,10]. For such marine application, the material of choice is Duplex Stainless Steel (DSS) because of its good mechanical properties and corrosion resistance [11]. This material consists of a two-phase microstructure: ferrite / austenite. The mechanical behavior and corrosion resistance are directly related to the microstructure of the material, and especially to the ferritic and austenitic phases distribution [12,13]. A phase ratio of approximately 50/50 is often desired to optimize the corrosion resistance, and heat treatments can be applied to achieve this phase distribution [14,15].

Current investigations on the processing of DSS via AM show that the target ferrite / austenite balance is not reached for as-deposited DSS [11]. Indeed, for most DSS obtained via powder-based AM, a high fraction of ferrite is observed, and austenite is only found at ferrite grain boundaries, such as Widmanstätten austenite or intragranular austenite [16,17]. This low austenite content is mainly due to the small heat input and the rapid cooling rate for powder-based AM [11,18,19]. However, for WAAM DSS, slow cooling rates in the temperature range 1200 −800 °C are favorable for austenite formation [20]. As a result, with commercial welding wires, a high fraction of austenite (≈ 74 %) is usually observed. Zhang *et al.* [21] confirmed this result using temperature measurements during WAAM process. Wittig *et al.* [20] showed that the decrease of arc energy can help to attain a phase balance close to 50/50. It is however observed that the spatial distribution of both phases is heterogeneous: a higher ratio of ferrite is found at the fusion lines between weld beads. Other studies show that the morphology of the austenite phase is also affected by the WAAM process, as it appears as either Widmanstätten austenite, intragranular austenite, or intergranular austenite depending on its position within the deposited layer [21,22]. Secondary austenite is also observed in some regions due to the cyclic thermal history during WAAM process [20,22].

The existence of microstructural heterogeneities induced by the AM scanning strategy is a classical observation for non-heat-treated AM materials [23–26]. These variations of microstructure induced by AM can lead to a singular mechanical behavior and preferential failure. Such

* Corresponding author.
E-mail address: lorenzo.bercelli@ensta-bretagne.fr (L. Bercelli).

https://doi.org/10.1016/j.matdes.2024.113223
Received 7 May 2024; Received in revised form 7 July 2024; Accepted 30 July 2024
Available online 31 July 2024

Nomenclature

ϕ	Additive manufacturing weaving angle
σ_y	Yield stress
σ_{ULT}	Ultimate tensile stress
A	Elongation to failure
θ	Temperature rise of a sample under cyclic loading
θ_d	Stabilized temperature rise linked to the material's inherent dissipative behaviour
θ^s_{the}	Temperature rise linked to the thermoelastic coupling
ρ	Density
c	Specific heat
$\vec{q}$	Local heat flux
C_{the}	Heat source of the thermoelastic coupling
Δ	Heat source of the inherent dissipation
T_0	Initial temperature
E	Young modulus
ν	Poisson coefficient
f_m	Mechanical frequency
α	Coefficient of thermal expansion
I_{1_a}	Amplitude of the stress tensor's first invariant
θ^s_1	First harmonic of the temperature linked to the thermoelastic coupling
$\mathcal{F}$	Fourier number
λ	Thermal conductivity
$\overline{l_c}$	Characteristic length of the smallest detectible I_1 gradient through thermoelastic stress analysis considering conduction effects
f_c	Camera sampling frequency
θ^e_1	First harmonic of the temperature linked to the thermoelastic coupling estimation based on infrared data
σ_{nom}	Nominal stress
$U_{y'}$	Displacement in direction $\vec{y'}$
ϵ_{yy}	Strain in direction $\vec{y}$
θ^{s*}_1	Reference temperature's first harmonic corresponding to a loading of amplitude σ^{nom}_a
k	Readjustment factor between experimental and expected theoretical temperatures

effect was investigated by Chen et al. [27], who observed systematic static failure in the so-called Heat Affected Zone (HAZ, *i.e.* the fusion line between layers) for a iron-based alloy obtained via WAAM. In the work by Popovich *et al.* [28] on an additively manufactured Inconel 718 with purposely induced microstructural variations, it was shown, using EBSD and Digitial Image Correlation (DIC), that grain size and texture had a direct impact on strain localization. In the work by Kale *et al.* [29] on a 316L stainless steel fabricated by Selective Laser Melting, DIC and EBSD analysis showed that deformation heterogeneities were induced by both crystallographic texture and the presence of pores. DIC analysis performed by Sun et al. [30] on a low-carbon steel fabricated by WAAM showed again the existence of regular strain concentration bands under uniaxial tension.

From this short literature review, it appears that materials fabricated by WAAM have a singular microstructure with strong heterogeneities depending on the scanning strategy, that induces heterogeneous mechanical behavior, as observed by DIC with the evidence of strain concentrations. However, the existence of such behavior in the elastic domain and its effect on preferential location for fatigue failure have not yet been observed. In this work, it is proposed to establish a correlation between a process induced microstructural pattern and a heterogeneous elastic behavior of a DSS manufactured by WAAM aimed for naval applications [31]. The aim is to propose a method to assess the effect and possible criticality of such microstructural patterns on structural components.

This paper is divided into three sections. First, details are given regarding the chemical composition and basic mechanical properties of the DSS obtained by WAAM used in this study. The experimental set-up is also presented, namely, microstructural analysis, DIC analysis and Thermoelastic Stress Analysis (TSA), from which the theoretical background is reminded. Second, the experimental results are presented: the presence of microstructural patterns is highlighted via both optical microscopy and EBSD; strain concentrations consistent with the literature are observed via DIC, and stress concentrations are found via TSA. Finally, the mechanical fields, both from DIC and TSA, are compared to macrographs, demonstrating the correlation between microstructural patterns and strain/stress concentrations. It is found that TSA is an adapted experimental technique to observe and assess the effect of a WAAM scanning strategy on the microstructure and thus the mechanical behavior.

2. Materials and methods

2.1. WAAM duplex stainless steel

The material of study is a duplex (austenitic-ferritic) stainless steel produced by WAAM via Gas Metal Arc Welding (GMAW) using Cold Metal Transfer (CMT) technology. The filler material is a regular DSS welding wire whose chemical composition is detailed in Table 1.

The material was provided in the form of multi-bead non-heat-treated blocks of dimensions $300 \times 210 \times 55mm$ produced by Ecole Centrale de Nantes (Fig. 1). A weaving deposition strategy is used for the fabrication of these blocks in which weld beads of each layer are orientated alternatively at angle $+\phi$ (denoted $\vec{x'}$) and $-\phi$ (denoted $\vec{x''}$) with respect to the transverse direction of the substrate $\vec{x}$ (Fig. 1 a). As a result, a very specific pattern of the weld beads appears:

- as $\pm\phi$ bands in the plane of a layer (x, y) (Fig. 1 b);
- as a "wave" pattern in an arbitrary vertical slice (x, z) (Fig. 1 c);
- or as an alternance of bands (in plane weld beads) and "waves" (out of plane weld beads) in vertical slice (x', z) where direction $\vec{x''}$ is orientated at $+\phi$ with respect to $\vec{x}$ (Fig. 1 d).

In the following, the plane of observation (x', z) is of particular interest. For clarity, a layer is referred to as l_i, where the subscript i is relative to the deposition process, with $i = 0$ corresponding to the first layer deposited on the substrate. Moreover, a difference is made regarding the orientation of weld beads within a layer with respect to the plane (x', z). Layers of welding direction $\vec{x'}$ are noted IP (In Plane) and layers of welding direction $\vec{x''}$ are noted OP (Out of Plane) (Fig. 1 d).

The mechanical properties of the WAAM DSS is determined via quasi-static uniaxial tensile tests on samples extracted along both the building direction $\vec{z}$ and the horizontal direction $\vec{y}$. As no significant anisotropy was found [21,22,32–34], only the mean values of the yield stress σ_y, the ultimate tensile stress σ_{ULT} and the elongation to failure A are given in Table 2.

2.2. Mechanical test samples

Samples are extracted from raw blocks via electrical discharge machining and mechanical machining, meaning that no effect of the as-

Table 1
Chemical composition of the filler material (Ugiweld 45 N) in weight percentage.

C (wt%)	Si (wt%)	Mn (wt%)	Ni (wt%)	Cr (wt%)	Mo (wt%)	Cu (wt%)	N (wt%)	S (wt%)	P (wt%)	Fe (wt%)
0.02	0.3–0.6	1.0–2.0	8.5–10.0	22.5–23.5	3.0–3.5	0.5	0.12–0.17	0.015	0.02	bal.

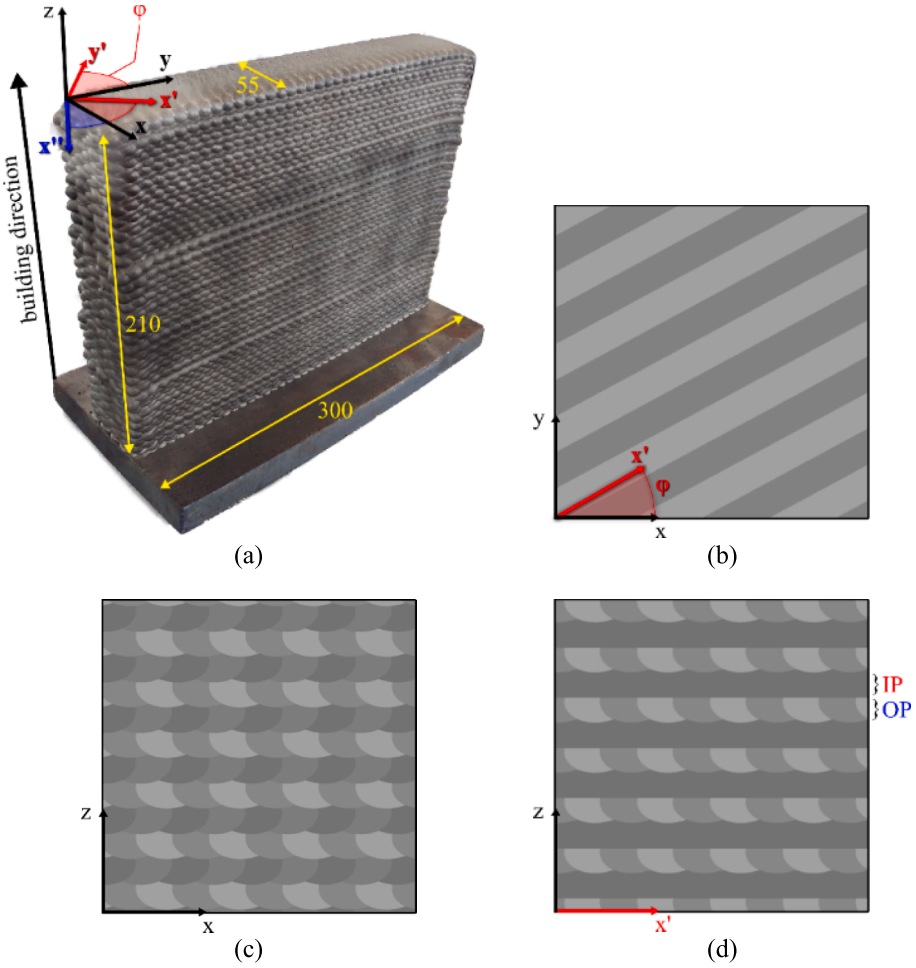

Fig. 1. Dimensions in millimetres of a raw WAAM DSS block (a), illustration of weld beads pattern in a layer (b), illustration of weld beads pattern in an vertical slice in the (x, z) plane (c) and illustration of weld beads pattern in a vertical slice orientated at $\pm\phi$ with respect to $\vec{y}$ in the (x', z) plane (d).

Table 2
Mean mechanical properties of the WAAM DSS.

σ_y(MPa)	σ_{ULT}(MPa)	A(%)
533	791	32

built rough surface is considered in this study. Two sample configurations are considered for mechanical testing (Fig. 2 a):

- Vertical samples (V) are extracted from raw material blocks so as to align the loading direction with the building direction $\vec{z}$ and the normal to the gauge section with $\vec{y'}$ (Fig. 1);
- Horizontal samples (H) are extracted from raw material blocks so as to align the normal to the gauge section with the building direction $\vec{z}$.

Both sample configurations are dog bone shaped, with the following gauge section dimensions: length 67*mm*, width 20*mm*, and thickness 6.5*mm* (Fig. 2 b). This corresponds to approximately to 5 −6 weld beads in width and approximately 33 layers in height for the V configuration.

2.3. Microstructural analysis

The specimen used for microstructural observations is a plate cut out in the core of the WAAM DSS block, with dimensions of 20 mm in the $\vec{x'}$ direction and 40 mm in the building direction $\vec{z}$. The studied surface of normal $\vec{y'}$ was carefully prepared prior to any observation. The specimen was mounted in a conductive resin and polished on a Struers LabPol machine using decreasing SiC papers and diamond pastes down to ¼ µm. Then, different preparation protocols were used depending on the experimental technique used for observation:

- Specimens for optical microscopy observations were etched using either
  - o a modified Beraha solution (60 mL H_2O + 30 mL HCl + 0.75 g of potassium bisulfite) applied during 10 s;
  - o a V2A etchant (100 mL H_2O + 100 mL HCl + 10 mL HNO_3) applied during 2 min;

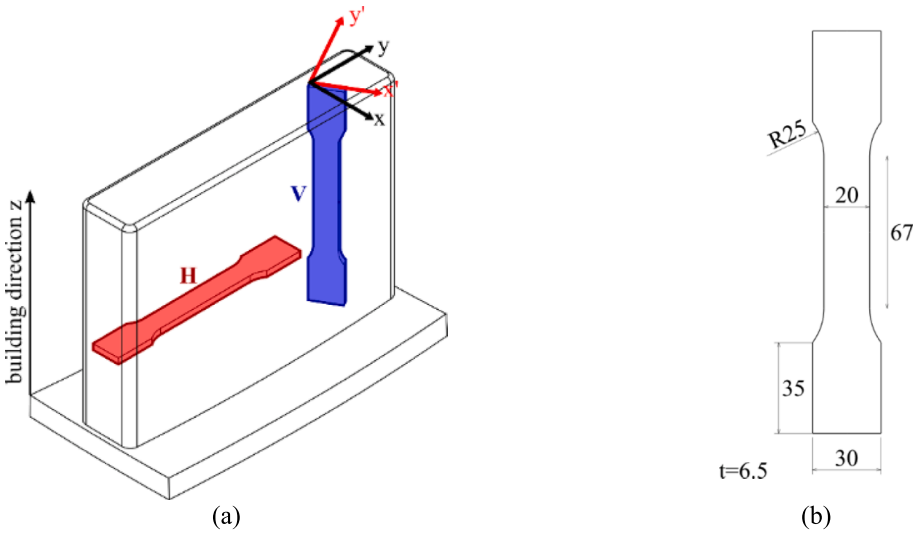

Fig. 2. Vertical (V) and horizontal (H) tensile test samples direction in the raw material block (a) and sample's dimensions in millimetres (b).

- Specimens aimed for SEM observations were polished using colloidal silica suspension without further chemical etching.

Microstructural observations were performed using both a Keyence VHX-5000 numerical microscope and a JEOL JSM-IT300LV Scanning Electron Microscope (SEM) fitted with Oxford Instruments Electron Back-Scattered Diffraction (EBSD) and Energy Dispersive X-Ray Spectroscopy (EDS) detectors.

2.4. Digital image correlation

In order to expose the existence of a heterogeneous strain field caused by the presence of microstructural patterns induced by the WAAM process, quasi-static tensile tests were performed under monitoring via Digital Image Correlation (DIC).

Tests are performed using a hydraulic tension–torsion testing machine with a 250*kN* load capacity. The tests are controlled in total strain using an extensometer until specimen failure. A black and white speckle pattern is added on the gauge section to allow for DIC measurement during the test (Fig. 3 a). DIC measurement and post-processing are performed using a GOM Aramis 3D camera (Fig. 3 b) and the GOM Aramis software.

Two samples are tested: one in the V configuration (S-V1) and one in the H configuration (S-H1). Samples are loaded until tensile failure, and images are regularly acquired with the GOM camera during the test to allow for DIC.

2.5. Thermoelastic stress analysis

Thermoelastic Stress Analysis (TSA) is an experimental method used to assess the stress field on the surface of a sample under cyclic loading in its elastic regime and based on the cyclic variation of its temperature. This method is especially efficient for the observation of stress heterogeneities, allowing the assessment of stress concentrations in assemblies or complex structures [35–37] as well as the detection and monitoring of fatigue cracks [38–41]. This experimental technique was chosen in this study to expose the existence of a heterogeneous stress field caused by the presence of microstructural patterns induced by the WAAM process.

2.5.1. Theoretical background of TSA

TSA relies on the measurement of the temperature response θ of a structure submitted to cyclic loading. This temperature response can be

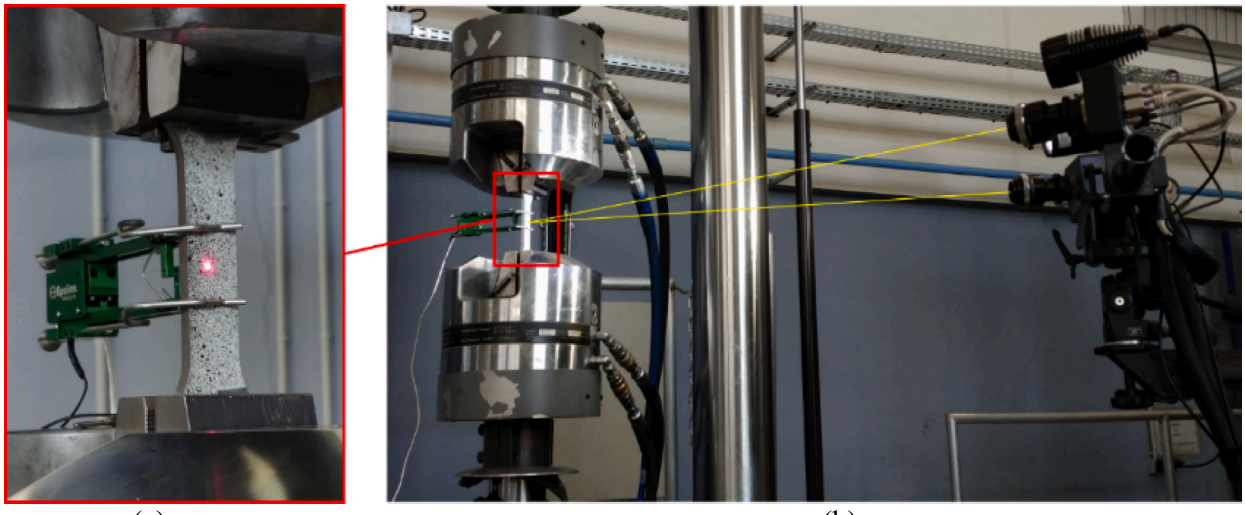

Fig. 3. Sample with speckle pattern and equipped with an extensometer mounted in the testing machine (a) and DIC test set-up with GOM Aramis 3D camera (b).

decomposed as follows (Fig. 4):

- an intrinsic dissipation to which is associated a progressive temperature rise θ_Δ
- the thermoelastic coupling to which is associated an immediate thermal response θ^s_{the} of the loaded structure.

For TSA, the thermoelastic coupling is of particular interest as the linked temperature allows for the stress field assessment on the observed surface. Indeed, the local heat equation states

$$\rho c \frac{\partial \theta}{\partial t} = -div(\vec{q}) + C_{the} + \Delta \tag{1}$$

where ρ is the density, c the specific heat, θ the temperature variation, $\vec{q}$ the local heat flux and C_{the} and Δ the heat sources of thermoelastic coupling and dissipation, respectively. Noting that, for small temperature variations θ (*i.e.* $\frac{\theta}{T_0} \ll 1$ where T_0 is the initial temperature), for typical steel materials at room temperature $\alpha^2 \frac{3E}{1-2\nu} T_0 \ll \rho c$ (with E the Young modulus) and considering a sinusoidal cyclic loading, the thermoelastic coupling heat source C_{the} can be written [42]

$$C_{the} = 2\pi f_m \alpha T_0 I_{1_a} \sin\left(2\pi f_m t - \frac{\pi}{2}\right), \tag{2}$$

where f_m is the mechanical loading frequency, α is the coefficient of thermal expansion, I_{1_a} is the amplitude of the stress tensor's first invariant and t the time. For linear problems (undamaged linear elastic materials) and under adiabatic condition, the temperature response linked to the thermoelastic coupling θ^s_{the} is also sinusoidal at frequency f_m and the corresponding temperature amplitude θ^s_1 (first harmonic of the temperature signal) is

$$\theta^s_1 = I_{1_a} \frac{\alpha T_0}{\rho c}. \tag{3}$$

As a result, the field of the temperature's first harmonic at frequency f_m is a direct image of the amplitude of the stress tensor's first invariant.

2.5.2. Conduction effect and smallest detectable stress field heterogeneity

In practice, the temperature response at the surface of a structure is assessed using an infrared camera. Infrared films are recorded over a chosen number of cycles over which the complete field of the experimental temperature first harmonic (at known frequency f_m) θ^e_1 on the observed surface is determined. It is important to note that the experimental temperature signal includes both the conduction effects and the surface emissivity. This means that the field of θ^e_1 assessed via infrared measurement is only an image of a locally averaged mechanical field I_{1_a} due to conduction effects. Indeed, testing conditions are not adiabatic given the material conductivity and the limited testing frequency $f_m = 10.02Hz$. Nevertheless, it is possible to estimate the extent of the conduction effect and the size of the smallest detectable heterogeneity $\overline{l_c}$ by calculating the Fourier number $\mathscr{F}$ [43]

$$\mathscr{F} = \frac{4\lambda}{\rho c f_m {l_c}^2}, \tag{4}$$

with λ the material thermal conductivity and l_c a characteristic length. Three cases can be considered depending on the value of $\mathscr{F}$:

- $\mathscr{F} \ll 1$: conduction effects are negligible;
- $\mathscr{F} = 1$: heating capacity and conduction are of the same order of magnitude;
- $\mathscr{F} \gg 1$: conduction is preponderant.

Imposing $\mathscr{F} = 1$, the value $\overline{l_c} = 1.4mm$ is determined, *i.e.* heterogeneities in the stress field of characteristic length greater than $1.4mm$ can be observed through TSA.

2.5.3. TSA test set-up

In order to expose the effect of the heterogeneous microstructure on the mechanical behaviour of WAAM DSS, cyclic tension tests in the elastic regime were performed and monitored using an infrared camera. The geometry dimensions of TSA samples are identical to those of monotonic tensile tests (Fig. 2). The same sample orientation configurations are also considered (V and H, Fig. 2 a). Samples gauge length are coated with a high-emissivity black paint.

Tests are performed using a hydraulic tension testing machine with a $250kN$ load capacity. The loading frequency f_m is chosen equal to $10.02Hz$. Tests are performed at a load ratio $R_F = \frac{F_{min.}}{F_{max}} = -1$ (zero mean stress). The infrared camera used in this study is a FLIR SC6700 with an image resolution of 640×512 pixels. Care is taken to cover both the sample and the infrared camera in a drape to avoid any interference from the testing environment (Fig. 5). The camera acquisition frequency f_c is set to $1Hz$. This generates a stroboscopic effect: the temperature linked to the thermoelastic coupling appears cyclic with a frequency f^{st}_m of $0.02Hz$ and a sampling of 50 points per cycle in films containing 3000 loading cycles. It allows for a fine assessment of the temperature amplitude θ^e_1 with less data space usage. The amplitude θ^e_1 of the temperature's first harmonic is estimated via a pixelwise fit of a function $f(t)$ expressed as the sum of a saturating exponential and a sine:

$$f(t) = T_0 + \theta_d \left[1 - \exp\left(-t/\tau_{eq}\right)\right] + \theta^e_1 \sin(2\pi f_m t + \phi), \tag{5}$$

where τ_{eq} is the characteristic time of thermal equilibrium. This post-processing of the infrared data is performed via the lab developed software Celenos [44].

In total, three samples are tested: two in the V configuration (S-V2 and S-V3) and one in the H configuration (S-H2). Tests are performed at five different cyclic loading levels for nominal stress amplitude σ_a between $100MPa$ and $300MPa$ (Table 3).

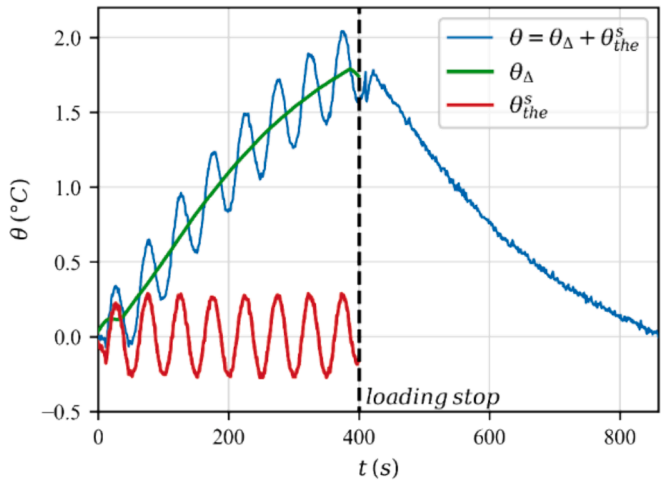

Fig. 4. Illustration of the temperature response θ of a WAAM DSS sample submitted to a cyclic loading.

3. Experimental results

3.1. Microstructural analysis

3.1.1. Optical observations

The material's microstructure is revealed via chemical etching, using the modified Beraha solution (see §2.3) for optical microscopy observations. A typical optical macrograph of the (x', z) plane (*i.e.* the V configuration, Fig. 2) is presented in Fig. 6 a, showing the microstructure of a zone covering roughly three layers (z direction) and three weld

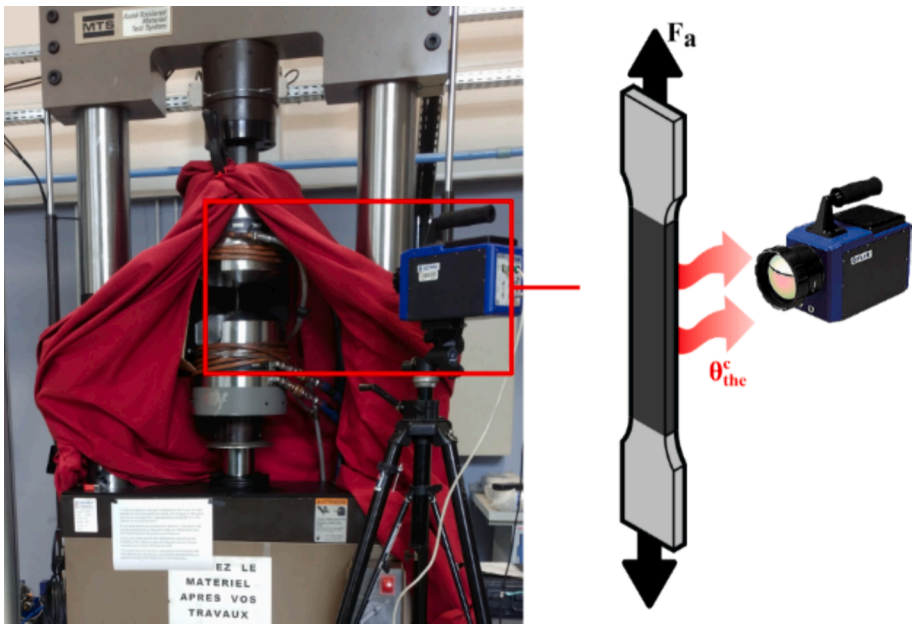

Fig. 5. Test set-up of the TSA under cyclic tension on a painted WAAM DSS sample.

Table 3
Nominal stress amplitude σ_a levels for the TSA tests.

Sample	σ_a(*MPa*)
S-V2	100 –150 –200 –250 –300
S-V3	100 –150 –200 –250 –300
S-H2	100 –150 –200 –250 –300

beads (x' direction). The microstructure appears to be heterogeneous: the deposition pattern of the (x', z) plane, as illustrated in Fig. 1 d, is made visible by variations in microstructure, grain size, and phase distribution. It must be noted that in the plane observation (x', z), if weld beads in the layer l_i are parallel to x' (IP layer), then weld beads in layers l_{i-1} and l_{i+1} are oriented along x'' (OP layers), hence the peculiar pattern. In Fig. 6 b, this pattern is drawn approximately on the micrograph for better comprehension: the interface between weld beads and/or layers is lightened, while the weld beads core is darkened.

To give better insight into the existence of such microstructural patterns, in Fig. 6, a focus is made on three specific zones, as defined in Fig. 6 b: Zone A in the core of a weld bead in an OP layer, Zone B in an interface between weld beads and layers, and Zone C in the core of a weld bead in an IP layer. Micrographs of Zone A, B and C are presented in Fig. 6 c, d and e respectively. All three zones display a typical DSS two-phase microstructure with austenite and ferrite (F). Austenite grains are arranged according to different classical microstructures that are found in all three zones, as indicated in Fig. 6, namely Widmanstätten Austenite (WA), Intragranular Austenite (IGA), formed inside ferrite grains, and Grain Boundary Austenite (GBA) appearing as elongated thin austenite grains found at the boundary of ferrite grains. However differences can also be observed when comparing the microstructures of the weld bead core (Zone A and Zone C) to the weld bead interface (Zone B):

- the weld bead core appears to be dominated by IGA and GBA, delimiting elongated macro ferritic grains, aligned with the normal of the weld bead interface (direction of maximum temperature gradient in the melt pool that tends to control an epitaxial grain growth [45,46]), as can be clearly observed in Zone A (Fig. 6 c);
- the weld bead boundary is dominated by an equiaxed WA microstructure, as found on top of solidified weld beads [47], making Zone B (Fig. 6 d) appear denser in the ferrite phase than Zone A and Zone C (Fig. 6 e).

In the (x, y) plane (*i.e.* the H configuration), microstructural patterns matching the WAAM deposition strategy (with weld tracks oriented at $\pm \phi$ with respect to $\vec{x}$) are also observed (Fig. 7 a). Tilted parallel bands are observed, which width depends on the position of the plane of observation within a deposited layer. In Fig. 7 b, this pattern is shown approximately for better comprehension: the interface between weld tracks is lightened, while the weld tracks core is darkened. As observed for the (x', z) plane (Fig. 6), these patterns are due both to heterogeneous distributions of ferrite and austenite and to the presence of different types of austenite grains arrangement. This is illustrated via a focus on three different zones: at the interface between weld tracks (Zone 1, Fig. 7 c) and in the core of two neighbouring weld tracks (Zone 2 in Fig. 7 d and Zone 3 in Fig. 7 e). The nature of the observed austenite grain arrangement depends on the position of the plane of observation within a deposited layer.

These observations are consistent with the literature on the welding or the WAAM of DSS [21,48–51]. In particular, it is found in [52] that the ferrite phase is denser at the interface between two consecutive weld beads (in the order of magnitude of 10% depending on the heat input).

3.1.2. *Electron BackScatter Diffraction (EBSD) analysis*

To confirm and elaborate on the optical observations, EBSD analysis was performed on the same sample as §3.1.1 for the (x', z) observation plane. Both phase distribution and grain orientation (Inverse Pole Figures, IPF) maps were constructed. Given the scale of WAAM microstructural patterns compared with the grain size, to ensure satisfactory grain indexation, an assembly of local EBSD maps was performed. To this end, the sample was first chemically etched for optical observation, and zones of interest were delimited using hardness prints. Then, the surface layer affected by chemical etching was removed via mechanical polishing using 1/4 μm diamond paste, followed by colloidal silica suspension polishing. Results are illustrated in Fig. 7.

An optical micrograph of the indented sample is shown in Fig. 7 a on which the EBSD zone of interest in OP layer l_n^{OP} is delimited in black; an optical micrograph of this zone of interest is shown in Fig. 7 b with indications of the weld bead interface and core regions. Because of the wide EBSD assembly, a slight spatial distortion of the image can be

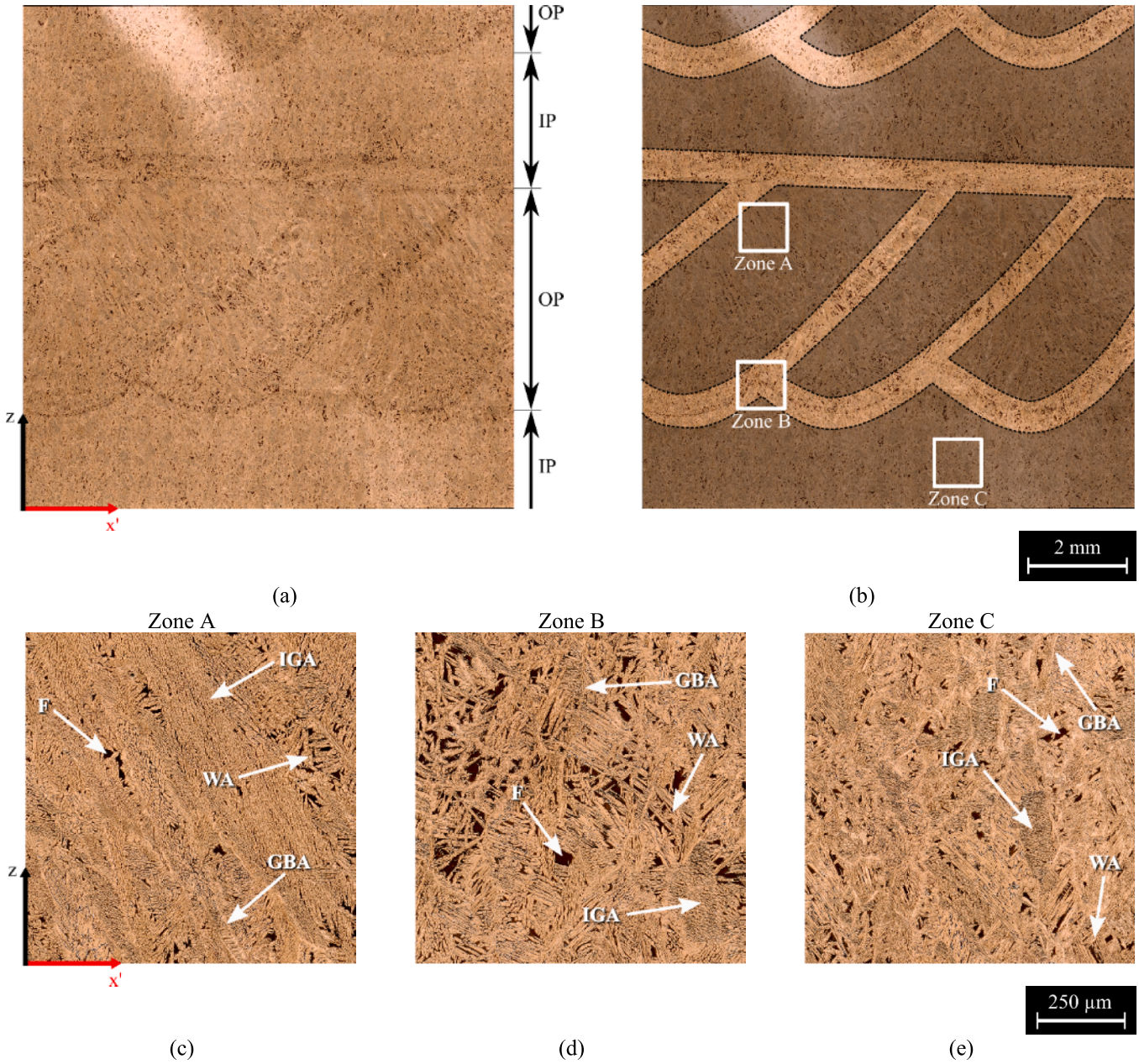

Fig. 6. Optical micrograph of the WAAM DSS in the (x', z) plane (V configuration) (a), highlight of the weld beads core and interface as well as zones of interest (b), micrographs of Zone A in the core of an OP layer weld bead (c), Zone B at the interface between weld beads and layers (d) and Zone C in the core of an IP layer weld bead (e) with indications of Ferrite (F), Widmanstätten Austenite (WA), Intra Granular Austenite (IGA) and Grain Boundary Austenite (GBA).

observed when comparing the optical image with the EBSD results. The occurrence of spatial distortion when constructing wide EBSD maps is a common issue [53,54], which is not limiting in the present study as only phase distribution and texture analysis are of interest.

The phase map (with ferrite in red and austenite in blue) obtained via EBSD analysis is presented in Fig. 7 c. An amount of ferrite of 11% is found according to the EBSD analysis, and a fraction of 75% of austenite. However, a value of roughly 29 % is measured via ferrite scope, which is found to be coherent with the amount of 26 % estimated via segmentation of the optical macrograph (Fig. 6 a) using a simple Otsu thresholding [55]. This difference with EBSD estimations is attributed to non-indexed data points, which seem to mostly correspond to ferrite grains (Fig. 7 c).

The grain orientation maps according to the deposition direction $\vec{z}$ are available for each phase individually (in Fig. 7 e for ferrite and Fig. 7 f for austenite) as well as for both phases (Fig. 7 d). It can be observed that elongated austenite grains in the direction of the maximum temperature gradient exist in the weld bead core region, as observed on optical micrographs. Smaller equiaxed austenite grains are present in the weld bead interface region (bottom right hand corner). In Fig. 7 e, ferrite macro-grains can be distinguished.

A texture analysis of the material's microstructure is performed via the processing of the Orientation Distribution Function (ODF) pole figure for crystallographic directions $\langle 100 \rangle$ according to the basis $(\vec{x''}; \vec{y''}; \vec{z})$ relative to the considered weld bead orientation. Results are illustrated in Fig. 8 for each phase. The crystallographic directions $\langle 100 \rangle$ are of particular interest as they correspond to the preferential directions of epitaxial growth of grains during welding [45–47]. Indeed, the result of such epitaxial growth can be observed on optical micrographs (Fig. 6) and EBSD maps (Fig. 7), in which elongated GBA and ferrite macro-

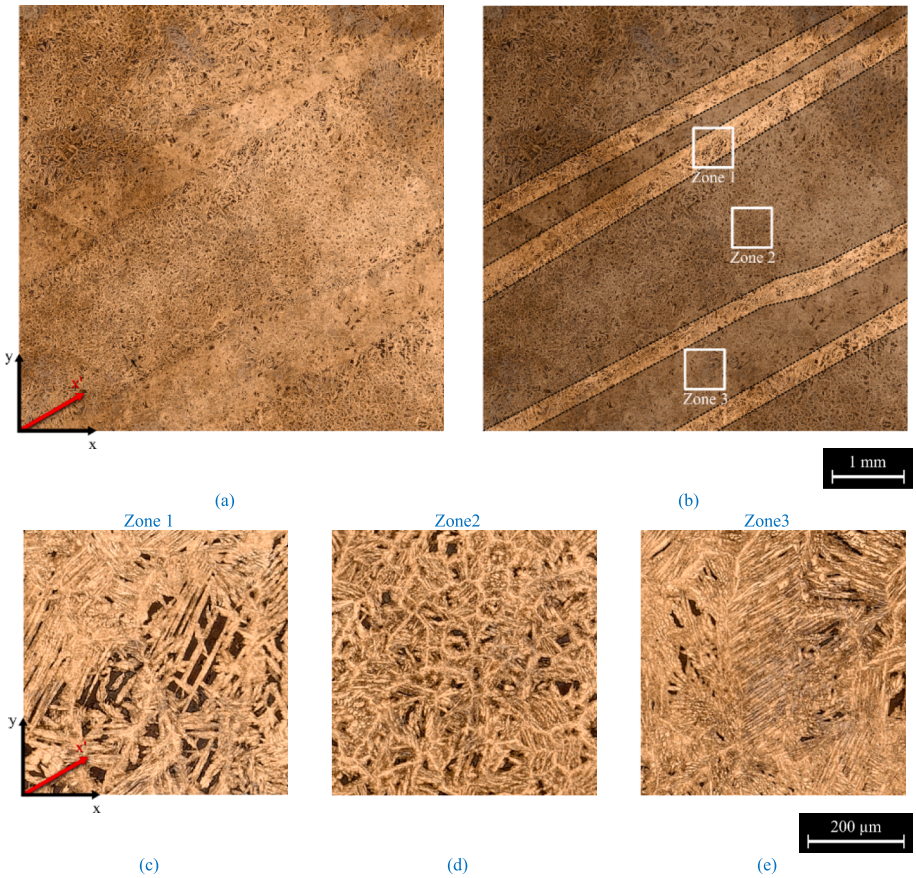

Fig. 7. Optical micrograph of the WAAM DSS in the (x, y) plane (H configuration) (a), highlight of the weld beads core and interface as well as zones of interest (b), micrographs of Zone 1 at the interface between weld tracks (c), Zone 2 in the core of a weld track (d) and Zone 3 in the core of a subsequent weld track (e).

grains are revealed, seemingly perpendicular to the weld bead interface, or more precisely parallel to the direction of the maximum temperature gradient in the weld pool. The ODF pole figure of ferrite (Fig. 8 a) reveals a strong texture, with concentrations about the $(y''; z)$ and $(x''; z)$ planes which are specific to the weld bead orientation in this analysed WAAM layer l_n. Despite the limited number of ferrite grains available in the zone analysed via EBSD, given their size relative to the size of one weld bead section, this ferrite texture is believed to be representative of the observed weld bead in its OP layer. Consequently, it can be expected that a different ferrite texture exists in layers l^{IP}_{n-1} and l^{IP}_{n+1}, given that their welding direction $\overrightarrow{x'}$ is different than $\overrightarrow{x''}$ of the analysed layer l^{OP}_n. On the other hand, no specific texture is exhibited for the austenite phase regarding to the $\langle 100 \rangle$ direction (Fig. 8 b).

3.2. Quasi-static tensile tests

Two samples (S-V1 and S-H1) were submitted to quasi-static tensile loading until failure. Mechanical field measurement was performed via DIC during the tests. The post-processing of DIC data revealed two singular fields: the out-of-plane displacement $U_{y'}$ of S-V1 and the longitudinal strain ϵ_{yy} of S-H1. The evolution of these two mechanical fields during the tensile tests is illustrated in Fig. 9 for nominal stresses $\sigma_{nom} = \frac{F_{nom}}{S_0}$ (with F_{nom} the applied load and S_0 the cross-sectional area) ranging from 500MPa to 800MPa.

The analysis of the out-of-plane displacement $U_{y'}$ of the sample S-V1 reveals the existence of a pattern of horizontal bands at stresses above the yield stress σ_y. Eight bands can be distinguished in the height of the region of interest at $\sigma_{nom} = 650MPa$ (Fig. 9 b). The number of observed bands is constant throughout the test, and their width appears to follow the global deformation of the sample as observed just before failure at $\sigma_{nom} = 765MPa$ (Fig. 9 c). Such pattern can hardly be observed at lower stress, for $\sigma_{nom} \leq \sigma_y$ (Fig. 9 a). This absence of a similar pattern in the measured mechanical field at $\sigma_{nom} \leq \sigma_y$ could be due to an insufficient DIC spatial resolution at lower strains.

Similar observations are made for sample S-H1 in the longitudinal strain ϵ_{yy} field, where tilted parallel bands appear, stacked along the sample's longitudinal direction $\overrightarrow{y}$ (Fig. 9 e). Their number is constant throughout the test, and their width as well as their orientation appears to follow the global deformation of the sample, as seen in the longitudinal strain field just before failure (Fig. 9 f). Again, this pattern can hardly be observed for lower stress levels, at $\sigma_{nom} \leq \sigma_y$ (Fig. 9 d).

3.3. Cyclic tensile tests

Three samples (S-V2, S-V3 and S-H2) were submitted to cyclic tension loading at a load ratio of $R_F = -1$ for different stress amplitudes below the macroscopic yield stress (Table 3). Fields of the temperature's first harmonic amplitude θ^c_1 on the gauge length are determined from infrared films for each stress level; the results are illustrated in Fig. 10. The colour range of temperature θ^c_1 maps is controlled through the definition of a reference temperature θ^{s*}_1

$$\theta^{s*}_1 = \sigma^{nom}_a \frac{\alpha T_0}{\rho c}, \tag{6}$$

and a factor k

$$k = \frac{\overline{\theta^c_1}^{ROI}}{\theta^{s*}_1}, \tag{7}$$

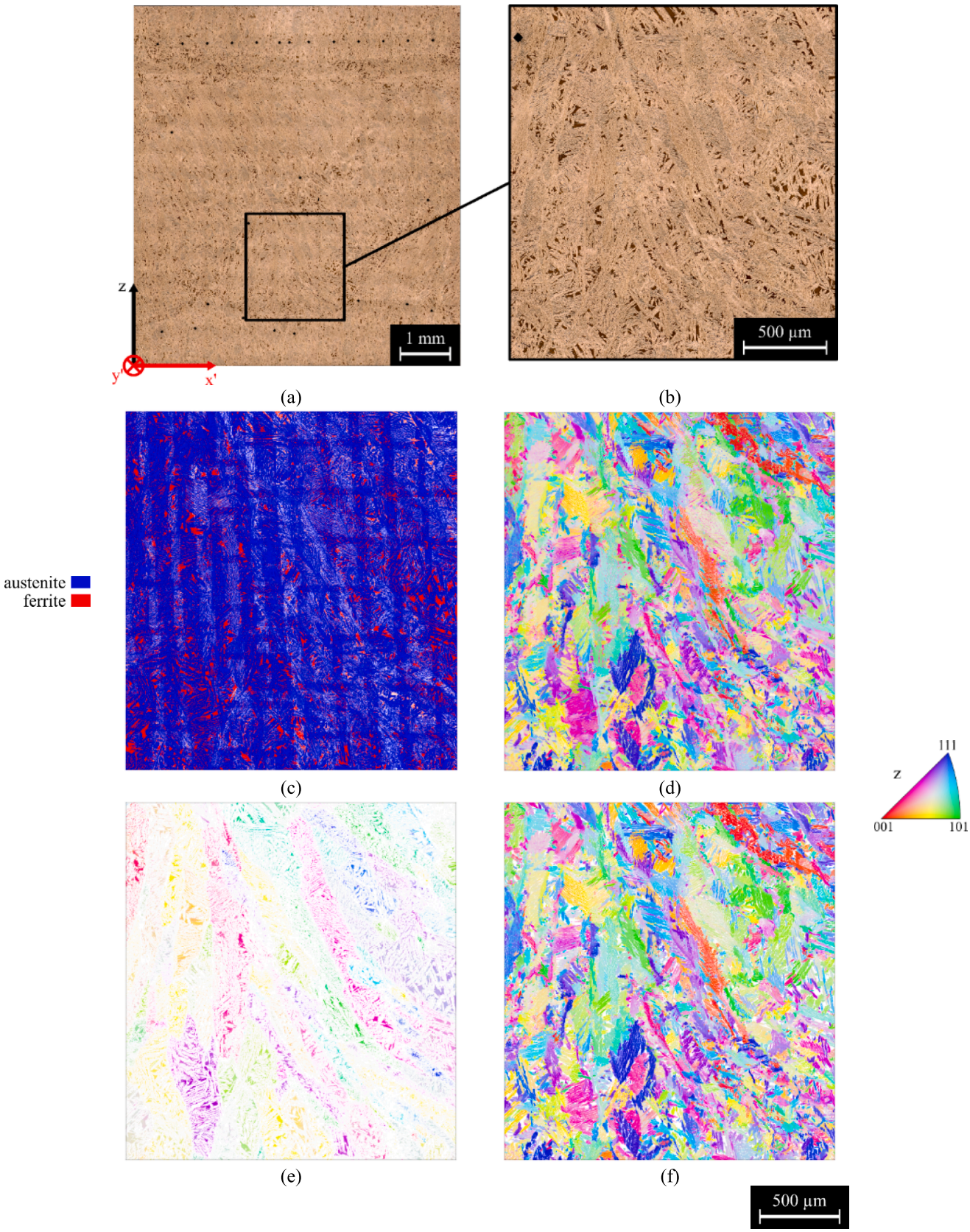

Fig. 8. Optical micrograph of the indented specimen prior to EBSD analysis (a), zoom on the region of interest to be analysed via EBSD (b), phase repartition map in the region of interest (c), grain orientation map (IPF *z*) of both ferrite and austenite phases in the region of interest (d), grain orientation map (IPF *z*) of the ferrite phase in the region of interest (e) and grain orientation map (IPF *z*) of the austenite phase in the region of interest (f).

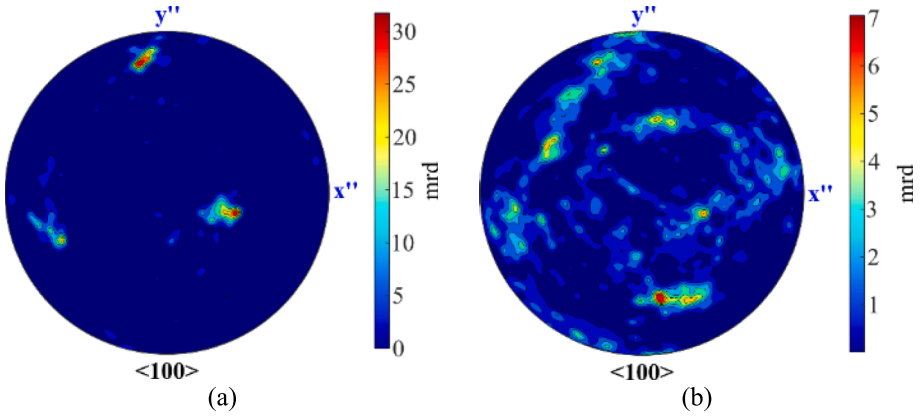

Fig. 9. ODF pole figures for the ferrite phase (a) and austenite phase (b) for crystallographic directions.⟨100⟩

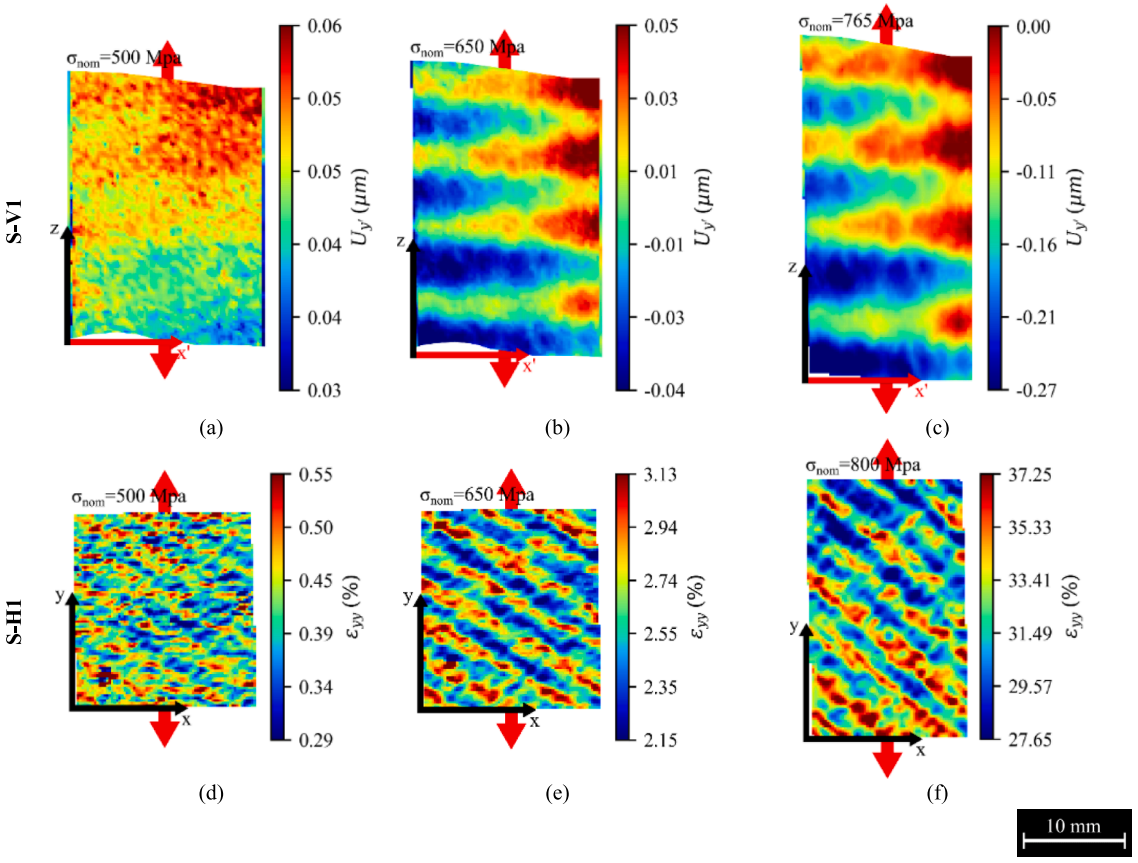

Fig. 10. DIC results on WAAM DSS samples in the V-configuration (out-of-plane displacement $U_{y'}$) for a nominal loading of 500*MPa* (a), of 650*MPa* (b), of 765*MPa* (c) and in the H-configuration (longitudinal strain ϵ_{yy}) for a nominal loading σ_{nom} of 500*MPa* (d), of 650*MPa* (e) and of 800*MPa* (f).

where $\sigma_a^{nom} = \frac{F_a^{nom}}{S_0}$ is the nominal stress amplitude (with F_a^{nom} the applied load amplitude and S_0 the cross-sectional area), and $\overline{\theta_1^c}^{ROI}$ is the average value of θ_1^c in the region of interest. $\theta_1^{s^*}$ corresponds to the theoretical temperature's first harmonic amplitude for an uniaxial loading of amplitude σ_a^{nom}, while k is a readjustment factor between experimental and theoretical temperatures due to experimental misconsiderations (black paint emissivity, infrared camera measurement noise, …). Such definition of the temperature range allows for the maps of θ_1^c to give information as to orders of magnitude of local stress gradients (in the sense of I_{1_a}). However, care should be taken not to interpret maps of θ_1^c as an accurate depiction of stress concentrations for the following reasons:

- the characteristic length of field heterogeneities at stake is too small to ignore conduction effects (see §2.5.2), which could lead to an underestimating of stresses [38];
- no motion compensation was applied prior to the pixelwise fit (see §2.5.3);
- the heterogeneities of θ_1^c could also be the result of material properties heterogeneities (namely α, ρ and c).

Nevertheless, the order of magnitude of stress concentration estimated via TSA (Fig. 10) is consistent with the literature as to the predominant effect of void defects on fatigue failure of machined WAAM specimens [56] or the predominant effect of surface condition on fatigue failure for as-built WAAM specimens [39,57–59].

It is observed that the heterogeneous field of θ_1^c constitutes a very specific pattern depending on the sample direction in the WAAM block. For the V configuration samples (S-V2 and S-V3), the pattern consists of two types of horizontal bands, alternating along the loading direction (building direction $\vec{z}$ of the WAAM block). One strip appears as a continuous line of high magnitude θ_1^c, the other appears as a juxtaposition of ellipses of low magnitude θ_1^c (Fig. 10 c). For the H-configuration sample (S-H2), the θ_1^c pattern consists of oblique bands oriented at 60° with respect to the loading direction (longitudinal direction $\vec{y}$ of the WAAM block, Fig. 10 c). It appears that a strong heterogeneity exists in the field of θ_1^c even for the lowest stress level, at $\sigma_a = 100MPa$. This heterogeneity appears slightly blurred for higher stress amplitudes: this is in large part attributed to the absence of motion compensation prior to the pixelwise identification of θ_1^c, leading to poor field measurement at larger strains.

4. Discussion

4.1. Comparison of DIC results with microstructural observations

As shown in §3.2, the post-processing of the DIC data acquired during monotonic tensile tests highlights the existence of mechanical field heterogeneities at high strains. The microstructure of the tested samples, after quasi-static tensile tests, is revealed using a V2A etchant (see §2.3). The characteristic dimensions of the DIC patterns, just before failure, appear to match the characteristic dimensions of the microstructural patterns of failed samples. For the sample in the vertical configuration S-V1, the striped pattern in the out-of-plane displacement field U_y before failure shows a characteristic length of approximately 8.5 mm (Fig. 11 a). The microstructure of the same sample, analysed after static failure, shows a band pattern with a comparable characteristic length, corresponding to the deposition layers, where some layers (in which weld beads are oriented along the normal to the plane of observation y) contain grains elongated along the tensile direction z (Fig. 11 a). The same correspondence is observed for the horizontal configuration sample S-H1, in which the mechanical field of longitudinal strain ϵ_{yy} just before failure and the microstructure after failure show similar patterns of orientated bands with a characteristic length of 3.8 mm (Fig. 11 b).

This tends to show that the mechanical field heterogeneities observed in the plastic domain of the WAAM material are caused by its specific microstructure, and so are due to the WAAM process. Similar observations were performed by Popovich et *al.* [28] who demonstrated that a heterogeneous microstructure purposely generated via AM leads to strong mechanical field heterogeneities observed by DIC in the plastic domain.

The highlighting of fine heterogeneities in the mechanical behaviour at such a scale through DIC is only achievable at high strains, *i.e.,* in the plastic domain. On the contrary, the use of TSA allows for the observation of the microstructure influence on the mechanical field in the elastic domain.

4.2. Comparison of TSA results with microstructural observations

As shown in 3.3, the DDS processed by WAAM exhibits a heterogeneous stress field (heterogeneous field of the amplitude of the temperature's first harmonic θ_1^c) in the elastic domain when submitted to simple uniaxial cyclic tension. It is suggested that such heterogeneities result from the heterogeneous microstructure of the material. Indeed, the evaluation of characteristic dimensions in both the stress field and the microstructure appears to be consistent. This is illustrated by the observation of the $(\vec{x}, \vec{z})$ plane in Fig. 12. The layer thickness is estimated to be 4.3 mm and the track width to be 2.8 mm (Fig. 12 a). Such values appear to match the characteristic dimensions in the patterns of the θ_1^c field, as illustrated on sample S-V3 for a stress amplitude of 150

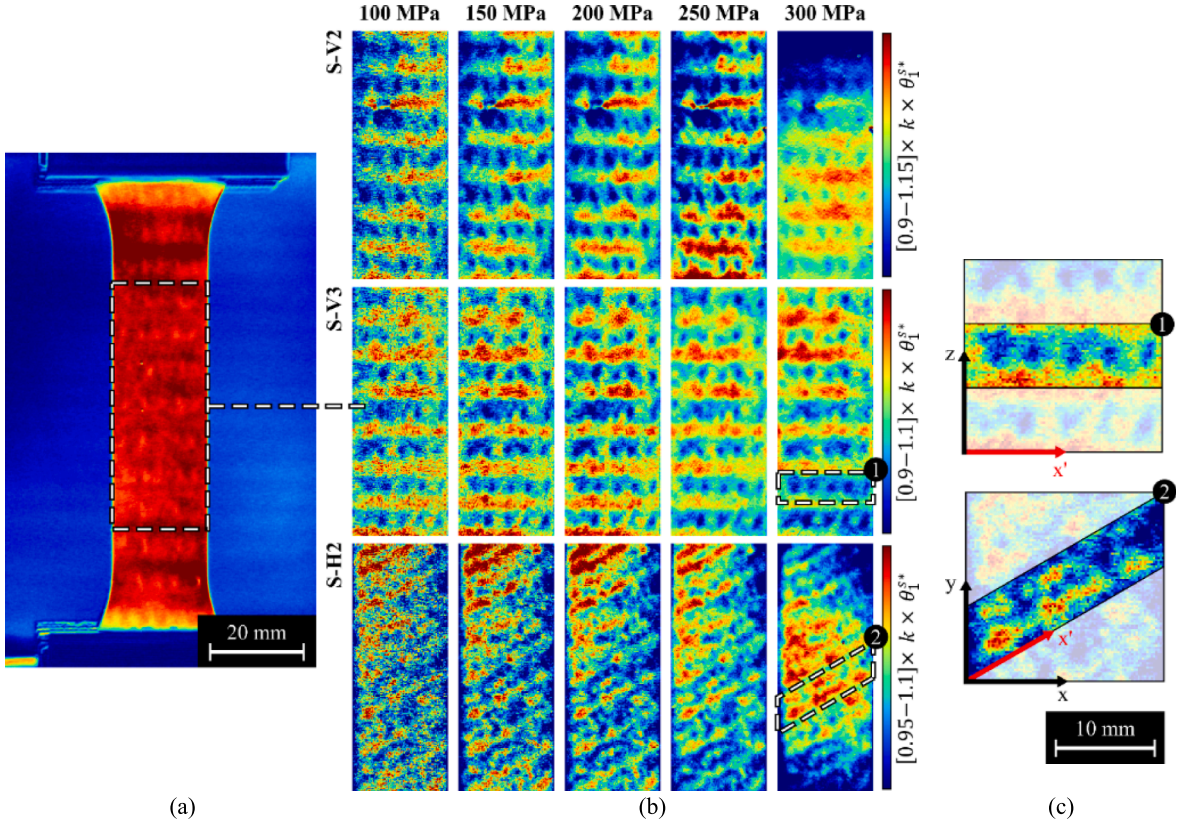

Fig. 11. Image of the temperature's first harmonic θ_1^c in the infrared camera field of view (a), images of the temperature's first harmonic θ_1^c in the gauge length of samples S-V2, S-V3 and S-H2 at different stress amplitudes (b) and zoom-in of the two different θ_1^c patterns (c).

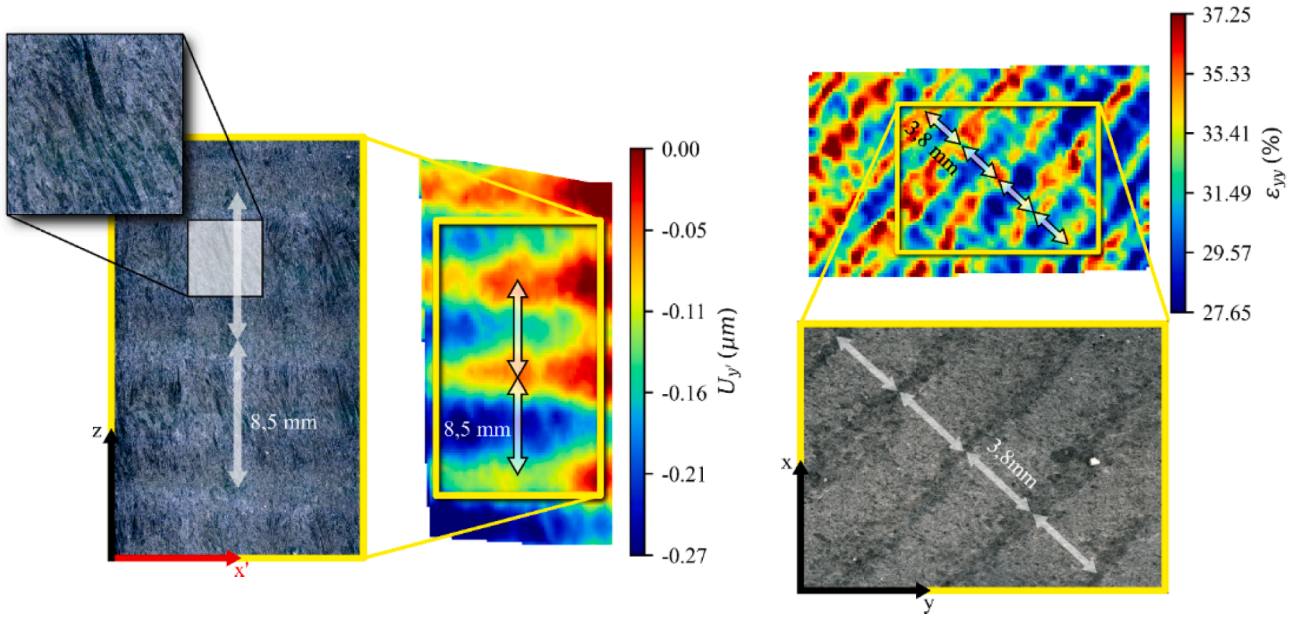

Fig. 12. Comparison of the microstructure after tensile failure with the out-of-plane displacement field $U_{y'}$ before failure of sample S-V1 (a) and with the longitudinal strain field ϵ_{yy} before failure of sample and S-H1 (b).

MPa (Fig. 12 b). As for the H configuration (horizontal plane $(\vec{x}, \vec{y})$), the field of θ_1^{ϵ} for sample S-H2 (Fig. 10 b) shows a pattern (oblique lines of constant θ_1^{ϵ} values) consistent with the microstructural pattern observed in the optical macrograph for such a sample (Fig. 11 b).

Following the expression of the amplitude of the temperature's first harmonic θ_1^{s} under perfect adiabatic conditions (equation (3), the difference in θ_1^{ϵ} (first harmonic's amplitude under experimental conditions) from one physical point to another can be explained by a difference in local stress I_{1_a} or by a difference in local material properties (namely ρ, c or α). Given that the core of weld beads from one layer to another contains identical microstructures and supposedly identical material properties, the patterns observed in the TSA field θ_1^{ϵ} is the result of differences in local stress I_{1_a}.

On the one hand, the banded pattern in θ_1^{ϵ}, with alternance of high θ_1^{ϵ} (red) and low θ_1^{ϵ} (blue), as shown in Fig. 12 b, is the result of differences in local stress I_{1_a} in consecutive layers caused by their distinct

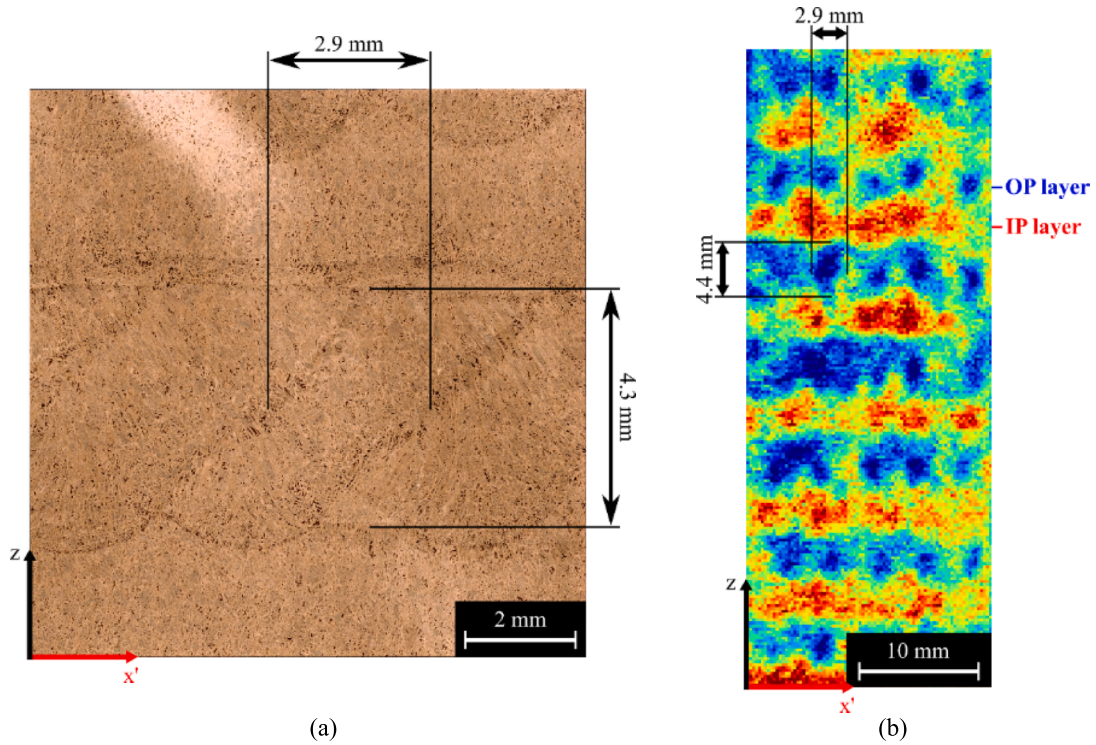

Fig. 13. Comparison of the microstructure's characteristic dimensions with that of the map of the amplitude of temperature's first harmonic θ_1^{ϵ} of the gauge length of sample S-V3 for a stress amplitude of 200 MPa.

preferential ferrite orientation (*cf.* §3.1.2), induced by the weld track orientation (and consecutive epitaxial growth of the grains), with respect to the loading direction (Fig. 13).

On the other hand, the wave-like pattern of θ_1^c, that exists within any OP layer (layers of low θ_1^c value), results from variations in the ferrite content along the width of the sample, with higher concentrations at the weld bead interface. Such ferrite content variation does not exist on the surface of the observation for IP layers; as a result, IP layers appear almost homogeneous (due to conduction effects with the surrounding OP layers) and are equal to high θ_1^c value bands in the TSA field. The effect of ferrite content variation on TSA fields can also be observed on the H specimen, where the red tilted band pattern corresponds to the high ferrite content weld bead interfaces in the (x, y) plane (Fig. 10 b).

5. Conclusion

This study investigated the microstructural effect of a DSS processed by WAAM on its mechanical behaviour, namely mechanical field heterogeneities under simple uniaxial loading. From the experimental results, the following observations are made:

1. Optical microscopy observations revealed that the WAAM DSS has a heterogeneous microstructure, showing patterns of characteristic dimension of a few millimetres, corresponding to that of the deposited weld beads. This microstructural pattern is due to the concentration of ferrite at the weld bead interface, the presence of an elongated GBA in the weld bead core aligned in the direction of the maximum temperature gradient inside the welding melt pool, and WA at the weld bead interface.
2. EBSD analysis revealed the existence of a texture for the ferrite phase, for which the $\langle 100 \rangle$ direction is preferably aligned with $\overrightarrow{y'}$ inside the deposited block. Such texture is attributed to the WAAM process, and its nature is presumably controlled by the deposition strategy (orientation of the weld beads within one deposited layer).
3. The DIC results under monotonic tensile loading revealed the existence of heterogeneous strain and displacement fields in the plastic regime. The heterogeneity patterns appeared to depend on the sample orientation according to the layer deposition direction with respect to the loading direction.
4. The comparison between DIC fields before sample failure and the optical observations of the failed sample's microstructure shows that the heterogeneity patterns are similar and have comparable characteristic dimensions.
5. The TSA results, under cyclic tensile loading at $R = -1$, revealed the existence of a heterogeneous stress field in the elastic regime. The heterogeneity patterns appeared to depend on the sample orientation according to the layer deposition direction with respect to the loading direction.
6. The comparison between TSA fields and the optical observations of the material's microstructure shows that the heterogeneity patterns are similar and have comparable characteristic dimensions. Both the inhomogeneity in ferrite distribution, and the different ferrite textures in consecutive layers can explain the TSA field pattern.

In conclusion, this study presented different experimental methods to assess the effect of WAAM microstructure on the mechanical behaviour of a DSS, namely DIC and TSA. While the existence of a correlation between microstructural heterogeneity and mechanical behaviour heterogeneity is no surprise, the present study shows that the scale at stake in the case of WAAM (a few millimetres) could come close to that of structural elements. Indeed, the material of the present study is aimed at the fabrication of hollow marine propeller blades [10]. In that regard, TSA appears to be a suitable method for the assessment of stress concentration levels associated with the existence of a heterogeneous microstructure obtained by WAAM, allowing for a quantitative analysis about WAAM layer deposition strategy's impact on the material's linear elastic behaviour.

CRediT authorship contribution statement

Lorenzo Bercelli: Writing – review & editing, Writing – original draft, Visualization, Investigation, Conceptualization. **Célia Caër:** Writing – review & editing, Writing – original draft, Visualization, Investigation, Conceptualization. **Matthieu Dhondt:** Writing – review & editing, Writing – original draft, Visualization, Investigation, Conceptualization. **Cédric Doudard:** Writing – review & editing, Conceptualization. **Julien Beaudet:** Writing – review & editing, Resources, Conceptualization. **Sylvain Calloch:** Writing – review & editing, Conceptualization.

Declaration of competing interest

The authors declare that they have no known competing financial interests or personal relationships that could have appeared to influence the work reported in this paper.

Data availability

The authors do not have permission to share data.

Acknowledgements

This study received funding from European Union's Horizon 2020 research and innovation program under grant agreement N°723246 as part of the RAMSSES project [31].

IRDL and ENSTA Bretagne gratefully acknowledge "Contrat de Plan Etat - Région Bretagne (CPER)" as well as the "Fonds Européen de Développement Régional (FEDER)" for their financial support to the reported work.

The authors would like to thank the GeM laboratory at Centrale Nantes for providing the material of study. This work was performed as part of Gustave Zédé joint lab collaborative research between Naval Group and ENSTA Bretagne.

References

[1] A. Bandyopadhyay, Y. Zhang, S. Bose, Recent developments in metal additive manufacturing, Curr. Opin. Chem. Eng. 28 (2020) 96–104, https://doi.org/10.1016/j.coche.2020.03.001.

[2] S. Pratheesh Kumar, S. Elangovan, R. Mohanraj, J.R. Ramakrishna, Review on the evolution and technology of State-of-the-Art metal additive manufacturing processes, Mater. Today Proc. 46 (2021) 7907–7920, https://doi.org/10.1016/j.matpr.2021.02.567.

[3] Y. Li, S. Yu, Y. Chen, R. Yu, and Y. Shi, "Wire and arc additive manufacturing of aluminum alloy lattice structure," *J. Manuf. Process.*, vol. 50, no. October 2019, pp. 510–519, 2020, doi: 10.1016/j.jmapro.2019.12.049.

[4] K. Refai, C. Brugger, M. Montemurro, N. Saintier, An experimental and numerical study of the high cycle multiaxial fatigue strength of titanium lattice structures produced by Selective Laser Melting (SLM), Int. J. Fatigue 138 (2020) 105623, https://doi.org/10.1016/j.ijfatigue.2020.105623.

[5] D. Ding, Z. Pan, D. Cuiuri, H. Li, A multi-bead overlapping model for robotic wire and arc additive manufacturing (WAAM), Robot. Comput. Integr. Manuf. 31 (2015) 101–110, https://doi.org/10.1016/j.rcim.2014.08.008.

[6] Q. Cui, H. Zhang, S. S. Pawar, C. Yu, X. Feng, and S. Qiu, "Topology Optimization for 3D-Printable Large-Scale Metallic Hollow Structures With Self-Supporting," *Proc. 27th Conf. Comput. Aided Archit. Des. Res. Asia [Volume 2]*, vol. 2, pp. 101–110, 2022, doi: 10.52842/conf.caadria.2022.2.101.

[7] J. L. McNeil, W. R. Hamel, J. Penney, A. Nycz, and M. Noakes, "Framework for CAD to part of large scale additive manufacturing of metal (LSAMM) in arbitrary directions," *Solid Free. Fabr. 2019 Proc. 30th Annu. Int. Solid Free. Fabr. Symp. - An Addit. Manuf. Conf. SFF 2019*, pp. 1126–1135, 2019.

[8] I. Tabernero, A. Paskual, P. Álvarez, A. Suárez, Study on arc welding processes for high deposition rate additive manufacturing, Procedia CIRP 68 (April) (2018) 358–362, https://doi.org/10.1016/j.procir.2017.12.095.

[9] C. Nota, G. Rückert, J.L. Heuzé, L. Carlino, J.M. Quenez, L. Courregelongue, A first feedback on manufacturing and in-service behaviour of a WAAM-made propeller for naval application, Weld. World 67 (4) (Apr. 2023) 1113–1121, https://doi.org/10.1007/s40194-023-01475-w.

[10] G. Pechet, J.-Y. Hascoet, M. Rauch, G. Ruckert, A.-S. Thorr, Manufacturing of a hollow propeller blade with WAAM process - from the material characterisation to the achievement, in: Industry 4.0 – Shaping the Future of the Digital World, CRC Press, 2020, pp. 155–160.
[11] D. Zhang, A. Liu, B. Yin, and P. Wen, "Additive manufacturing of duplex stainless steels - A critical review," *J. Manuf. Process.*, vol. 73, no. August 2021, pp. 496–517, 2022, doi: 10.1016/j.jmapro.2021.11.036.
[12] H. Hwang, Y. Park, Effects of heat treatment on the phase ratio and corrosion resistance of duplex stainless steel, Mater. Trans. 50 (6) (2009) 1548–1552, https://doi.org/10.2320/matertrans.MER2008168.
[13] M.H. Jang, J. Moon, T.H. Lee, S.J. Park, H.N. Han, Effect of nitrogen partitioning on yield strength in nitrogen-alloyed duplex stainless steel during annealing, Metall. Mater. Trans. A Phys. Metall. Mater. Sci. 45 (4) (2014) 1653–1658, https://doi.org/10.1007/s11661-014-2210-8.
[14] Y. Yang, et al., Effect of annealing temperature on the pitting corrosion behavior of UNS S82441 duplex stainless steel, Corrosion 69 (2) (Feb. 2013) 167–173, https://doi.org/10.5006/0717.
[15] Z. Zhang, et al., Effect of post-weld heat treatment on microstructure evolution and pitting corrosion behavior of UNS S31803 duplex stainless steel welds, Corros. Sci. 62 (2012) 42–50, https://doi.org/10.1016/j.corsci.2012.04.047.
[16] A.D. Iams, J.S. Keist, T.A. Palmer, Formation of Austenite in additively manufactured and post-processed duplex stainless steel alloys, Metall. Mater. Trans. A 51 (2) (Feb. 2020) 982–999, https://doi.org/10.1007/s11661-019-05562-w.
[17] M. Brázda, P. Salvetr, J. Dlouhý, and J. Vavrík, "Influence of laser power in direct laser deposition on the proportion of ferrite and austenite in duplex steel saf2507," *Met. 2020 - 29th Int. Conf. Metall. Mater. Conf. Proc.*, no. January 2022, pp. 539–544, 2020, doi: 10.37904/metal.2020.3517.
[18] K. Davidson, S. Singamneni, Selective laser melting of duplex stainless steel powders: an investigation, Mater. Manuf. Process. 31 (12) (2016) 1543–1555, https://doi.org/10.1080/10426914.2015.1090605.
[19] F. Hengsbach, et al., Duplex stainless steel fabricated by selective laser melting - Microstructural and mechanical properties, Mater. Des. 133 (2017) 136–142, https://doi.org/10.1016/j.matdes.2017.07.046.
[20] B. Wittig, M. Zinke, S. Jüttner, Influence of arc energy and filler metal composition on the microstructure in wire arc additive manufacturing of duplex stainless steels, Weld. World 65 (1) (2021) 47–56, https://doi.org/10.1007/s40194-020-00995-z.
[21] Y. Zhang, S. Wu, F. Cheng, A specially-designed super duplex stainless steel with balanced ferrite:austenite ratio fabricated via flux-cored wire arc additive manufacturing: Microstructure evolution, mechanical properties and corrosion resistance, Mater. Sci. Eng. A vol. 854, no. June (2022) 143809, https://doi.org/10.1016/j.msea.2022.143809.
[22] P.P. Nikam, D. Arun, K.D. Ramkumar, N. Sivashanmugam, Microstructure characterization and tensile properties of CMT-based wire plus arc additive manufactured ER2594, Mater. Charact. vol. 169, no. July (2020) 110671, https://doi.org/10.1016/j.matchar.2020.110671.
[23] C. Guévenoux, S. Hallais, A. Charles, E. Charkaluk, A. Constantinescu, Influence of interlayer dwell time on the microstructure of Inconel 718 Laser Cladded components, Opt. Laser Technol. 128 (August) (2020), https://doi.org/10.1016/j.optlastec.2020.106218.
[24] M. Froend, V. Ventzke, F. Dorn, N. Kashaev, B. Klusemann, and J. Enz, "Microstructure by design: An approach of grain refinement and isotropy improvement in multi-layer wire-based laser metal deposition," *Mater. Sci. Eng. A*, vol. 772, no. January 2020, p. 138635, 2020, doi: 10.1016/j.msea.2019.138635.
[25] S. Kiakidis, "Mechanical and corrosion behaviour of 3D printed aluminium bronzes produced by wire+arc additive manufacturing. In Collaboration with RAMLAB", Delft University, 2017.
[26] S. Raghavan, et al., Effect of different heat treatments on the microstructure and mechanical properties in selective laser melted INCONEL 718 alloy, Mater. Manuf. Process. 32 (14) (2017) 1588–1595, https://doi.org/10.1080/10426914.2016.1257805.
[27] W. Chen, H. Cao, L. Zhu, Heterogeneous microstructure and anisotropic mechanical properties of reduced activation ferritic/martensitic steel fabricated by wire arc additive manufacturing, Nucl. Mater. Energy 33 (2022) 101261, https://doi.org/10.1016/j.nme.2022.101261.
[28] V.A. Popovich, E.V. Borisov, A.A. Popovich, V.S. Sufiiarov, D.V. Masaylo, L. Alzina, Functionally graded Inconel 718 processed by additive manufacturing: Crystallographic texture, anisotropy of microstructure and mechanical properties, Mater. Des. 114 (2017) 441–449, https://doi.org/10.1016/j.matdes.2016.10.075.
[29] A.B. Kale, J. Singh, B.-K. Kim, D.-I. Kim, S.-H. Choi, Effect of initial microstructure on the deformation heterogeneities of 316L stainless steels fabricated by selective laser melting processing, J. Mater. Res. Technol. 9 (4) (2020) 8867–8883, https://doi.org/10.1016/j.jmrt.2020.06.015.
[30] L.H.S. Fabricated, L. Sun, F. Jiang, R. Huang, D. Yuan, C. Guo, Microstructure and mechanical properties of low-carbon high-strength steel fabricated by wire and arc additive manufacturing, Metals (basel) (2020).
[31] "Realisation and Demonstration of Advanced Material Solutions for Sustainable and Efficient Ships," 2017. https://www.ramsses-project.eu/ (accessed Apr. 14, 2020).
[32] A. Queguineur, J. Marolleau, A. Lavergne, G. Rückert, Evaluation of tandem controlled short-circuit GMAW for improved deposition in additive manufacture of large Nickel Aluminium Bronze naval components, Weld. World 64 (8) (2020) 1389–1395, https://doi.org/10.1007/s40194-020-00925-z.
[33] Z. Qiu, et al., Microstructure and mechanical properties of wire arc additively manufactured Hastelloy C276 alloy, Mater. Des. 195 (2020) 109007, https://doi.org/10.1016/j.matdes.2020.109007.
[34] A. Horgar, H. Fostervoll, B. Nyhus, X. Ren, M. Eriksson, and O. M. Akselsen, "Additive manufacturing using WAAM with AA5183 wire," *J. Mater. Process. Technol.*, vol. 259, no. November 2017, pp. 68–74, 2018, doi: 10.1016/j.jmatprotec.2018.04.014.
[35] P. Florin, C. Doudard, M. L. Facchinetti, and S. Calloch, "Determination of the First Stress Tensor Invariant of a Complex Steel Sheet Structure from Thermoelastic Stress Analysis Determination of the first stress tensor invariant of a complex steel sheet structure from Thermoelastic Stress Analysis," *Procedia Eng.*, vol. 133, no. January 2016, pp. 736–745, 2015, doi: Doi: 10.1016/j.proeng.2015.12.655.
[36] D. Palumbo, U. Galietti, Characterisation of steel welded joints by infrared thermographic methods, Quant. Infrared Thermogr. J. 11 (1) (2014) 29–42, https://doi.org/10.1080/17686733.2013.874220.
[37] L. Navrátil, et al., Understanding the damage mechanisms in 3D layer-to-layer woven composites from thermal and acoustic measurements, J. Compos. Mater. 56 (10) (2022) 1559–1575, https://doi.org/10.1177/00219983221077331.
[38] L. Carteron, C. Doudard, S. Calloch, B. Levieil, J. Beaudet, F. Bridier, Naval welded joints local stress assessment and fatigue cracks monitoring with quantitative thermoelastic stress analysis, Theor. Appl. Fract. Mech. 110 (Dec. 2020) 102792, https://doi.org/10.1016/j.tafmec.2020.102792.
[39] L. Bercelli, C. Doudard, S. Calloch, V. Le Saux, and J. Beaudet, "Thermometric investigations for the characterization of fatigue crack initiation and propagation in Wire and Arc Additively Manufactured parts with as-built surfaces," *Fatigue Fract. Eng. Mater. Struct.*, vol. 46, no. 1, p. 153:170, 2022.
[40] L. Bercelli, B. Levieil, B. Malek, F. Bridier, and A. Ezanno, "Use of infrared thermography to model the effective stress ratio effect on fatigue crack growth in welded T -joints," *Eng. Fract. Mech.*, vol. 279, no. September 2022, pp. 1–17, 2023, doi: 10.1016/j.engfracmech.2023.109061.
[41] R. De Finis, D. Palumbo, F. Di Carolo, M. Ricotta, G. Meneghetti, U. Galietti, Crack tip position evaluation and Paris' law assessment of a propagating crack by means of temperature-based approaches, Procedia Struct. Integr. vol. 39, no. C (2021) 528–545, https://doi.org/10.1016/j.prostr.2022.03.126.
[42] T. Boulanger, A. Chrysochoos, C. Mabru, A. Galtier, Calorimetric analysis of dissipative and thermoelastic effects associated with the fatigue behavior of steels, Int. J. Fatigue 26 (3) (2004) 221–229, https://doi.org/10.1016/S0142-1123(03)00171-3.
[43] W. Rohsenow, J. Hartnett, Y. Cho, Handbook of Heat Transfer, 3rd ed., McGraw Hill, 1998.
[44] V. Le Saux, C. Doudard, Infrared Physics and Technology Proposition of a compensated pixelwise calibration for photonic infrared cameras and comparison to classic calibration procedures: Case of thermoelastic stress analysis, Infrared Phys. Technol. 80 (2017) 83–92, https://doi.org/10.1016/j.infrared.2016.11.008.
[45] S. Kou, Y. Le, Nucleation Mechanisms and Grain Refining of Weld Metal, Weld. J. (miami, Fla) 65 (12) (1986) pp.
[46] L. Ji, J. Lu, C. Liu, C. Jing, H. Fan, and S. Ma, "Microstructure and mechanical properties of 304L steel fabricated by arc additive manufacturing," vol. 03006, 2017, doi: 10.1051/matecconf/201712803006.
[47] J. Liu, A.C. To, Quantitative texture prediction of epitaxial columnar grains in additive manufacturing using selective laser melting, Addit. Manuf. 16 (2017) 58–64, https://doi.org/10.1016/j.addma.2017.05.005.
[48] X. Bi, R. Li, Z. Hu, J. Gu, C. Jiao, Microstructure and Texture of 2205 Duplex Stainless Steel Additive Parts Fabricated by the Cold Metal Transfer (CMT), Wire Arc Addit. Manufactur. (WAAM) (2022), https://doi.org/10.3390/met12101655.
[49] K. Wu, et al., Effect of variable polarity during cold metal transfer on microstructure and mechanical properties of directed energy deposition-arc built 2209 duplex stainless steel, Addit. Manuf. 75 (2023) 103750, https://doi.org/10.1016/j.addma.2023.103750.
[50] Y. Zhang, F. Cheng, and S. Wu, "The microstructure and mechanical properties of duplex stainless steel components fabricated via flux-cored wire arc-additive manufacturing," *J. Manuf. Process.*, vol. 69, no. January 2020, pp. 204–214, 2021, doi: 10.1016/j.jmapro.2021.07.045.
[51] Y. Yuan, R. Li, X. Bi, J. Gu, and C. Jiao, "Experimental and Numerical Investigation of CMT Wire and Arc Additive Manufacturing of 2205 Duplex Stainless Steel," 2022.
[52] V.A. Hosseini, M. Högström, K. Hurtig, M.A. Valiente Bermejo, L.E. Stridh, L. Karlsson, Wire-arc additive manufacturing of a duplex stainless steel: thermal cycle analysis and microstructure characterization, Weld. World 63 (4) (2019) 975–987, https://doi.org/10.1007/s40194-019-00735-y.
[53] V. S. Tong and T. Ben Britton, "TrueEBSD: Correcting spatial distortions in electron backscatter diffraction maps," *Ultramicroscopy*, vol. 221, no. October 2020, p. 113130, 2021, doi: 10.1016/j.ultramic.2020.113130.
[54] G. Nolze, Image distortions in SEM and their influences on EBSD measurements, Ultramicroscopy 107 (2–3) (2007) 172–183, https://doi.org/10.1016/j.ultramic.2006.07.003.
[55] N. Otsu, A threshold selection method from gray-level histograms, IEEE Trans. Syst. Man. Cybern. 9 (1) (Jan. 1979) 62–66, https://doi.org/10.1109/TSMC.1979.4310076.
[56] L. Bercelli, S. Moyne, M. Dhondt, C. Doudard, S. Calloch, J. Beaudet, A probabilistic approach for high cycle fatigue of Wire and Arc Additive Manufactured parts taking into account process-induced pores, Addit. Manuf. 42 (June) (2021) 2021, https://doi.org/10.1016/j.addma.2021.101989.
[57] H. Bartsch, R. Kühne, S. Citarelli, S. Schaffrath, M. Feldmann, "Fatigue analysis of wire arc additive manufactured (3D printed) components with unmilled surface,"

Structures, vol. 31, no. November 2020, pp. 576–589, 2021, doi: 10.1016/j.istruc.2021.01.068.

[58] K. Samadian, W. De Waele, W. de Waele, Fatigue crack growth model incorporating surface waviness for wire+arc additively manufactured components, Procedia Struct. Integr. 28 (2019) (2020) 1846–1855, https://doi.org/10.1016/j.prostr.2020.11.008.

[59] M. Renault, L. Bercelli, C. Doudard, B. Levieil, J. Beaudet, S. Calloch, Infrared imaging surface roughness criticality assessment of Wire Arc Additive Manufactured specimens, Procedia Struct. Integr. 57 (2022) (2024) 22–31, https://doi.org/10.1016/j.prostr.2024.03.004.